Journal of Nuclear Materials 540 (2020) 152373

Contents lists available at ScienceDirect

Journal of Nuclear Materials

journal homepage: www.elsevier.com/locate/jnucmat

High-pressure structural behavior and elastic properties of U_3Si_5: A combined synchrotron XRD and DFT study

Jason L. Baker [a, **], Gaoxue Wang [b, ***], Tashiema Ulrich [c], Josh T. White [c], Enrique R. Batista [b], Ping Yang [b], Robert C. Roback [a], Changyong Park [d], Hongwu Xu [a, *]

[a] Earth and Environmental Sciences Division, Los Alamos National Laboratory, Los Alamos, NM, 87545, United States
[b] Theoretical Division, Los Alamos National Laboratory, Los Alamos, NM, 87545, United States
[c] Materials Science and Technology Division, Los Alamos National Laboratory, Los Alamos, NM, 87545, United States
[d] High-Pressure Collaborative Access Team, X-Ray Science Division, Argonne National Laboratory, Argonne, Illinois, 60439, United States

HIGHLIGHTS

- Bulk and axial moduli of U_3Si_5 were determined by high-pressure X-ray diffraction combined with diamond anvil cell technique.
- U_3Si_5 exhibits an anisotropy in compressibility with its *c*-axis being 2.2 times more compressible than the *a*-axis.
- Density functional theory was used to calculate the elastic parameters of U_3Si_5, which agree with the experimental values.

ARTICLE INFO

Article history:
Received 8 April 2020
Received in revised form
15 May 2020
Accepted 29 June 2020
Available online 10 July 2020

Keywords:
Uranium silicide
Crystal structure
Bulk modulus
High pressure
Synchrotron X-ray diffraction
Diamond anvil cell
Density functional theory

ABSTRACT

We present an integrated experimental and theoretical study of the structural behavior of U_3Si_5 at high-pressure conditions using angle-dispersive synchrotron X-ray diffraction (XRD) in a diamond anvil cell (DAC) and density functional theory (DFT) calculations. On increasing pressure, the ambient hexagonal structure of U_3Si_5 with space group *P6/mmm* remains stable up to 16.7 GPa, the maximum pressure tested with DAC. The bulk modulus and the *a*- and *c*-axial moduli of U_3Si_5 were experimentally determined to be 126 ± 4 GPa, 173 ± 8 GPa and 79.7 ± 4.3 GPa, respectively. Thus an anisotropy in the axial compressibility of U_3Si_5 is observed with its *c*-axis being more compressible than the *a*-axis. Our DFT calculation results are in general agreement with the experimental values, including reproducing the compressibility anisotropy. A comparison of the bulk modulus of U_3Si_5 to those of other U–Si compounds reveals a general trend that the bulk modulus of U–Si decreases with increasing U/(U + Si) ratio.

1. Introduction

Light Water Reactors (LWR) commonly rely on uranium dioxide (UO_2) as the nuclear fuel choice. However, in recent years, motivated by mitigation of Fukushima-like nuclear reactor disasters, potential accident-tolerant nuclear fuels such as uranium silicides (U–Si) have garnered a great deal of interest due to their higher thermal conductivities at operating temperatures [1–7]. The U–Si binary system consists of several well-defined, line compounds including U_3Si, U_3Si_2, U_3Si_5, USi, USi_2, USi_3 and $USi_{1.88}$ [8,9]. Although U_3Si_5 has a lower uranium density than some of the other U–Si phases, several advantages have been identified such as the neutronic similarity between a UN-U_3Si_5 composite and UO_2, which would minimize LWR operational differences and improve oxidation resistance compared to U_3Si_2, another U–Si fuel candidate [10]. Additionally, U_3Si_5 exhibits higher thermal conductivities than UO_2 above 600 K [2] and has the highest melting point (2043 K) among U–Si phases [8], which are favorable for nuclear fuel performance [11]. Despite the lower uranium density of this material compared to some other U–Si phases as well as UO_2, the other advantages of U_3Si_5 warrant detailed studies of its physical and chemical properties at relevant conditions (*e.g.*, pressure,

* Corresponding author.
** Corresponding author.
*** Corresponding author.
E-mail addresses: jlbaker@lanl.gov (J.L. Baker), gaoxuew@lanl.gov (G. Wang), hxu@lanl.gov (H. Xu).

https://doi.org/10.1016/j.jnucmat.2020.152373
0022-3115/

temperature) to further assess its applicability. Moreover, pressure is a powerful means to tune physical properties of materials, as structural transformations may occur at elevated pressures, which can lead to modified electronic structures in addition to the new crystalline structures produced [12,13]. Due to the importance of understanding the structural and mechanical stability of nuclear fuel materials at high-pressure conditions, it is necessary to perform measurements and simulations at these conditions on U_3Si_5.

U_3Si_5 crystallizes in a hexagonal structure with the space group *P6/mmm* (No. 191) at ambient conditions, and a model of this structure is shown in Fig. 1 [14,15]. This structure can be described as a defective AlB_2 type, which has a 5/6 Si occupancy [15]. As of this publication, no experimental high-pressure studies of structural behavior of U_3Si_5 have been performed. Some other U–Si phases such as USi and USi_2 have been examined at high-pressure conditions [16]. The structural behaviors of these two phases were explored up to 52 and 26 GPa, respectively, by Yagoubi et al., and they observed no pressure-induced phase transitions [16]. They also characterized the evolution of unit-cell parameters, and obtained high-pressure compressibility information through determination of the bulk moduli [16]. Additionally, U_3Si_2 was observed to remain in its ambient crystal structure at high-pressure conditions by Guo et al. [17] up to 37.6 GPa by synchrotron XRD measurements enabling the determination of bulk modulus and other elastic parameters. U_3Si_2 has an anisotropy in compressibility where its *c*-axis contracts more readily than its *a*-axis [17]. For U_3Si_5, although no experimental high-pressure studies have been conducted, Zhang et al. and Baskes et al. performed DFT calculations to determine its mechanical properties (*e.g.*, bulk modulus, shear modulus) [18,19].

As mechanical properties of nuclear fuel materials are important to assess their safe and effective use at reactor conditions, it is imperative to conduct such measurements on U_3Si_5 to provide a more complete understanding of the high-pressure elastic properties of these accident-tolerant nuclear fuels. Thus, in this study, we performed high-pressure powder XRD measurements on U_3Si_5 up to 16.7 GPa, yielding its unit-cell parameters at high pressures and its bulk and axial moduli. To complement these measurements, DFT calculations were also performed to derive the elastic properties of U_3Si_5, and the calculated results are in general agreement with those obtained experimentally.

2. Methods

2.1. Sample synthesis

The starting materials used in preparation of the U_3Si_5 sample were a high purity feedstock of depleted uranium plate and 99.999% purity silicon purchased from Alfa Aesar. U_3Si_5 buttons were prepared by arc-melting the uranium and silicon feedstock in a tri-arc furnace (5 TA Reed Tri-Arc, Centorr Vacuum Industries, USA) using synthesis procedures described previously [2]. The dominant phase was determined to be U_3Si_5 by use of ambient XRD with identification of minor UO_2 phase and a few peaks due to an unknown phase [2]. Other characterization techniques such as scanning electron microscopy were used to investigate the microstructure of the synthesized material, and the thermodynamic properties of this sample were also measured [2,20].

The buttons were crushed and ground in an inert atmosphere glove-box, and the particulates were put through a 325 mesh sieve in order to isolate smaller grains for use in our high-pressure XRD experiments. The grain sizes of the particulates were on the order of 20–40 μm.

2.2. High-pressure X-ray diffraction experiments and data analysis

High-pressure XRD experiments were performed at the Advanced Photon Source (APS), Argonne National Laboratory. Data were collected at the 16-BM-D beamline of the High-Pressure Collaborative Access Team (HPCAT) using a Princeton-type symmetric diamond anvil-cell (DAC). The sample was loaded into the DAC under an Ar-gas atmosphere (with a constant flow of 5 psi) and the O_2 level was monitored (kept below 0.5% as determined by an O_2 meter) throughout the loading process to minimize possible oxidation of the sample. More specifically, a small amount (approximately 10 μg) of the powder sample was loaded into a 150 μm hole of a 45 μm-thick pre-indented stainless steel gasket in the DAC with 300 μm diameter diamond-culets. The gasket hole was drilled using the laser-drilling system at HPCAT [21]. In addition, several ruby pieces were loaded along with the sample powders to serve as a pressure marker. Pressure was applied by a He gas membrane system at the beamline, and pressure was determined by measuring the spectral shift of the R1 fluorescence line of ruby excited by a 542 nm laser and using the standard ruby pressure scale [22]. A solution of 4:1 methanol: ethanol was used as

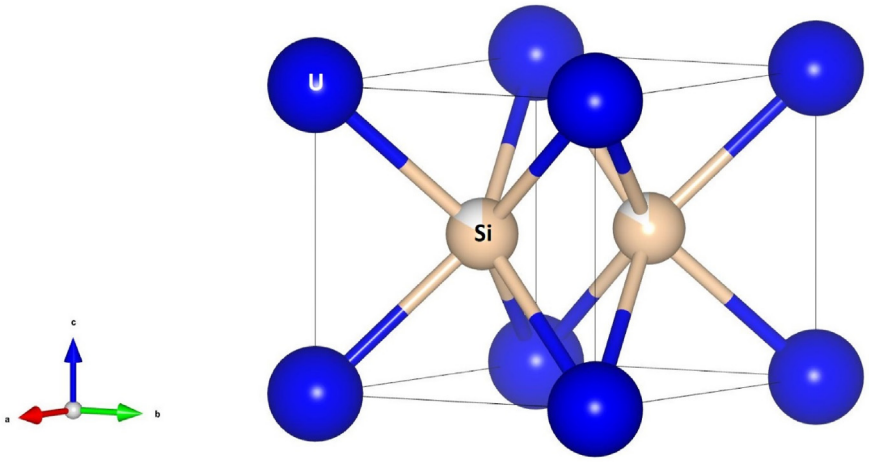

Fig. 1. Representative crystal structure (space group *P6/mmm*) of U_3Si_5. The white colored portion of the Si atom represents the inherent Si deficiency of 1/6 (i.e. Si occupancy of 5/6).

liquid pressure-transmitting media (PTM). This solution was chosen as the ideal liquid PTM for this experiment, since gas-loading options were not available due to the restrictions placed on handling radioactive materials at APS. 4:1 methanol: ethanol solution has been widely used in the high-pressure community and is generally considered quasi-hydrostatic in the pressure range of interest [23]. After loading of the sample and sealing the DAC, Kapton tapes were wrapped around the outside of the cell to provide two layers of containment of the sample (the first layer of containment is the diamond-gasket enclosure) to meet safety requirements for measuring radioactive samples at APS. Additionally, Kapton tapes were placed on the top and bottom of the DAC to enclose the area underneath each diamond, and on the top an optically clear Mylar window was included to allow for the measurements of ruby spectra for pressure determination.

An incident monochromatic X-ray beam was focused to a 5 μm spot-size onto the sample using Kickpatrick-Baez mirrors with a wavelength of 0.30966 Å. A MAR-345 imaging plate allowed collection of high-quality powder XRD patterns, and the detector distance was calibrated using a CeO_2 standard. After recording the Debye-Scherrer rings, the images collected were integrated and corrected for distortions using Dioptas software, which produced integrated intensity versus 2θ XRD plots [24]. To determine the unit-cell parameters of U_3Si_5 as a function of pressure, Le Bail analysis was performed on the integrated XRD patterns with the Rietica (LHPM) software package [25–27]. Fittings of the equations of state (EOS) based on the obtained unit-cell parameters to derive the bulk and axial moduli of U_3Si_5 were performed with the EOS-Fit7 program [28,29].

2.3. Density functional theory (DFT) calculations

All calculations were performed using DFT + U and projector augmented-wave (PAW) method as implemented in the Vienna Ab-initio Simulation Package (VASP) [30,31]. The generalized gradient approximation (GGA) of Perdew-Burke-Ernzerhof (PBE) functional with a Hubbard U term for uranium 5f electrons was used to correct the self-interaction errors in standard GGA exchange-correlation functional [32,33]. We used DFT + U with an effective U value of 1.5 eV [20], which has been demonstrated to yield reasonable structure and formation enthalpy for U–Si system [34]. Plane wave basis sets with a cutoff energy of 520 eV were employed [29]. The energy convergence was set to 10^{-6} eV. The Brillouin zone (BZ) was sampled with Monkhorst-Pack (MP) meshes with a density around 40 *k*-points per Å. For high-pressure calculations, hydrostatic pressure was applied to the structure and the force on each atom was converged to 0.01 eV/Å. No symmetry constraints were imposed during structural optimization. We have used the ferromagnetic (FM) ordering for all the considered structures, although U_3Si_5 exhibits paramagnetic behavior down to 4.2 K [35]. We have also performed one antiferromagnetic (AFM) calculation for one of the structures. It is found that the magnetic order has small influence on the relative lattice constants of U_3Si_5 at high pressures and thus also on its elastic properties.

3. Results and discussion

3.1. High-pressure XRD

The collected XRD patterns as a function of pressure are shown in Fig. 2. With increasing pressure, continuous shifts in the XRD peaks to higher 2θ are observed, which is indicative of continually decreasing unit-cell parameters, i.e., unit-cell contraction. Additionally, the absence of any major changes in the XRD patterns (i.e., no emergence, disappearance, or splitting of XRD peaks) suggests

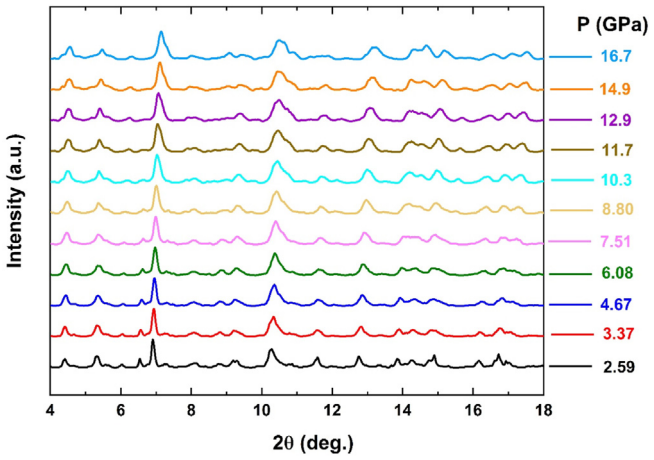

Fig. 2. Integrated X-ray diffraction patterns of U_3Si_5 collected on compression to 16.7 GPa.

that U_3Si_5 does not undergo any pressure-induced structural phase transition up to the maximum pressure (16.7 GPa) reached in this study. Decrease in intensity and broadening of peaks become more distinct above ~11 GPa, as the sample chamber becomes less hydrostatic with increasing pressure in the 4:1 methanol: ethanol PTM [23].

In Fig. 3, the XRD pattern collected at the lowest pressure (2.59 GPa) is shown, along with indexing of the peaks to the dominant U_3Si_5 phase (model depicted in Fig. 1) and a minor impurity phase, UO_2 (space group $Fm\bar{3}m$ (No. 225)) [36]. All peaks except the four peaks marked with an * are accounted for with these two phases. The marked peaks are from an unknown phase, which was previously observed in synthesis of U_3Si_5 [2]. However, as these peaks do not overlap with any reflections of U_3Si_5, they are not included in the analysis performed. Additionally, except for shifts to higher 2θ due to unit-cell contraction at 2.59 GPa, all peaks agree well with the ambient pressure XRD pattern collected

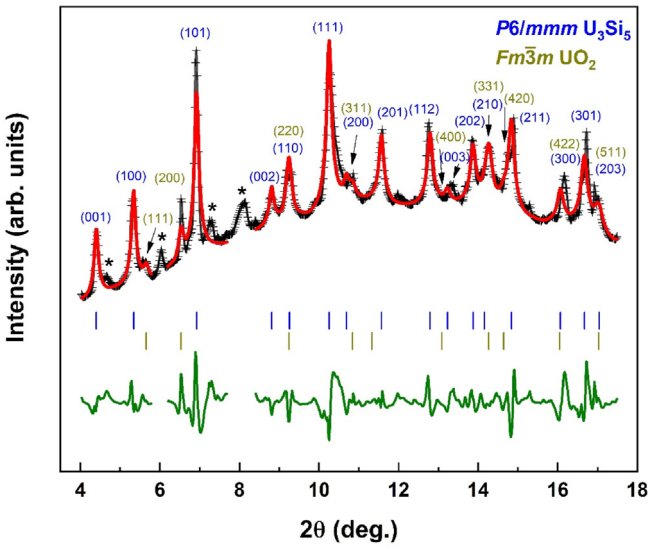

Fig. 3. Le Bail analysis of the XRD pattern collected at 2.59 GPa. The indicated *hkl* indices are for the major U_3Si_5 phase (blue) and a minor UO_2 phase (olive). The peaks labelled with an (*) are from a minor unknown phase. (For interpretation of the references to color in this figure legend, the reader is referred to the Web version of this article.)

previously [2]. Furthermore, Le Bail analysis was performed on this pattern and all other high-pressure XRD patterns in order to determine unit-cell parameters, *a* and *c*, which are listed in Table 1 [25,26]. The *c/a* ratio can be used as a parameter to describe the difference between the structures of U_3Si_5 and USi_2 where a *c/a* ratio greater than one indicates U_3Si_5 [37]. From the values in Table 1, it is evident that the *c/a* ratio remains larger than one at all pressures, indicating the U_3Si_5 structure [37]. It should also be noted that since data analysis was restricted to Le Bail analysis, the model occupancy of the Si site was unaccounted for in our analysis. However, as Le Bail analysis is a whole-pattern fitting approach, the unit-cell parameters can be derived accurately for each XRD pattern. Rietveld refinement, while ideal, was not possible due to the large grain sizes of the loaded sample leading to spotty 2D XRD images. The grain sizes were approximately 20–40 μm as a 325 mesh was used to separate ground material. The Le Bail analysis plot (Fig. 3) shows a good agreement between the observed and fitted XRD patterns, as indicated by the small residuals. The fitting agreement indices R_p and R_{wp} are 1.37% and 2.20%, respectively (Table 1).

3.2. Axial linear moduli

In order to characterize the evolution of the unit-cell parameters and cell volume of U_3Si_5 with pressure, Le Bail analysis was performed for each pressure on the corresponding XRD pattern. From these analyses, the unit-cell parameters at each pressure were determined and are presented in Table 1 along with the calculated unit-cell volume for the hexagonal structure using these lattice parameters. The estimated standard deviation (ESD) for the cell parameters determined from analysis of each XRD pattern is also given in Table 1 and this ESD is propagated using error analysis to determine the corresponding ESD for the unit-cell volume. The agreement indices R_p and R_{wp} are included for each fit to indicate the "goodness of fit" for each pattern.

Fig. 4 presents the variation of unit-cell parameters of U_3Si_5 (normalized to the fitted ambient pressure cell parameters a_0 and c_0) as a function of pressure. Upon initial inspection, it is clear that the *c*-axis contracts more readily than the *a*-axis. Quantification of this difference in compressibility can be achieved by fitting the data to the following equations [38]:

$$P = \frac{3M_{a,0}}{2}\left[\left(\frac{a_0}{a}\right)^7 - \left(\frac{a_0}{a}\right)^5\right] P = \frac{3M_{c,0}}{2}\left[\left(\frac{c_0}{c}\right)^7 - \left(\frac{c_0}{c}\right)^5\right] \quad (1)$$

where P is pressure, $M_{a,0}$ and $M_{c,0}$ are the axial linear moduli for the *a*- and *c*-axis, respectively, *a* and *c* are the unit-cell parameters measured at a given pressure (Table 1), and a_0 and c_0 are the unit-cell parameters at ambient pressure. By fitting the values in Table 1 to Equation (1), values of 173 (8) GPa and 79.7 (4.3) GPa are determined for $M_{a,0}$ and $M_{c,0}$, respectively (Table 2). As the axial compressibility is inversely proportional to the axial moduli, the *c*-axis of U_3Si_5 is 2.2 times more compressible than the *a*-axis. Additionally, it should be noted that the *c/a* ratio decreases from 1.046 at 2.59 GPa to 1.032 at 16.7 GPa, indicating a significant anisotropy, though reduced at high pressures.

Table 1
Unit-cell parameters and unit-cell volumes of U_3Si_5 at high pressures.

Pressure (GPa)	*a* (Å)	*c* (Å)	*V* (Å^3)	R_p (%)	R_{wp} (%)
2.59 ± 0.13	3.845 (1)	4.023 (2)	51.50 (4)	1.37	2.20
3.37 ± 0.17	3.836 (1)	4.018 (2)	51.19 (4)	1.39	2.27
4.67 ± 0.23	3.834 (1)	4.005 (2)	50.72 (4)	1.43	2.26
6.08 ± 0.30	3.812 (1)	3.994 (2)	50.27 (4)	1.50	2.20
7.51 ± 0.38	3.807 (1)	3.976 (2)	49.91 (4)	1.61	2.27
8.80 ± 0.44	3.801 (1)	3.960 (2)	49.54 (4)	1.64	2.24
10.3 ± 0.5	3.795 (1)	3.936 (2)	49.08 (4)	1.70	2.22
11.7 ± 0.6	3.786 (1)	3.923 (2)	48.70 (4)	1.84	2.42
12.9 ± 0.7	3.780 (1)	3.910 (2)	48.37 (4)	1.94	2.61
14.9 ± 0.7	3.765 (1)	3.884 (2)	47.68 (4)	1.67	2.55
16.7 ± 0.8	3.748 (2)	3.867 (2)	47.05 (6)	1.75	2.78

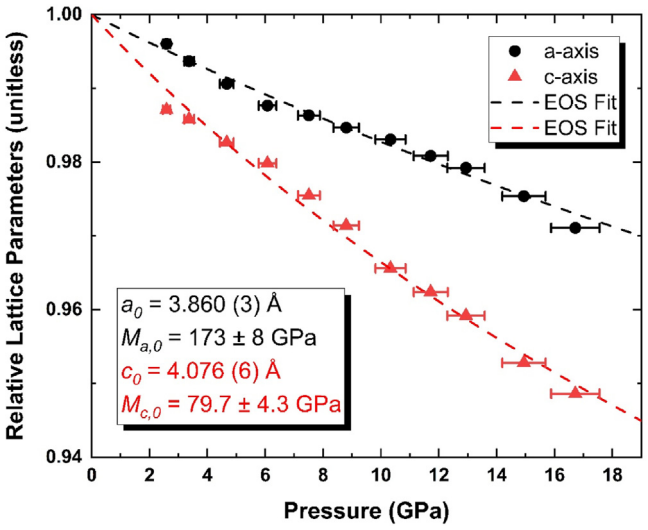

Fig. 4. Relative lattice parameters as a function of pressure. Fitted lines indicate equations of state for the *a-axis* (circle) and *c-axis* (triangle) using a linear 2nd order Birch-Murnaghan equation of state. The obtained parameters of the fits are given in the bottom inset.

DFT calculations were performed to provide insight into this compressibility anisotropy. Because the Si sites are partially occupied in U_3Si_5, various structures have been proposed for U_3Si_5 in the literature [15,18,39]. To capture its mechanical behavior, three ordered structures and two SQS (Special Quasirandom Structure) structures were used in our calculations. The first ordered structure is AlB_2-type USi_2 [*P6/mmm*, Fig. 5(a)]. This structure represents USi_2 without Si vacancy. The second and third structures are derived from the AlB_2-type USi_2 structure with different distributions of Si vacancies (Fig. 5(b and c)). The calculated relative lattice constants at high pressures are shown in Fig. 5(d, e, f), and the derived elastic properties of the ordered structures are summarized in Table 3. The SQS structures were produced with the ICET package [40]. The atomic coordinates and calculated energies of these structures, in the form of VASP POSCAR files, can be found in Table S1 in the supporting materials. It is found that the two SQS structures cannot correctly reproduce the mechanical properties of U_{3Si5} since the calculated *c*-axis is stiffer than the *a*-axis (contrary to our experimental result described above). A SQS structure with a much larger supercell is possibly required to reproduce the mechanical properties of U_3Si_5, which is computationally more demanding. The ordered structure shown in Fig. 5(b) has been widely used in the literature to model U_3Si_5 [18]. However, we found that the *c*-axis of this structure is stiffer than the *a*- and *b*-axis (crystallographically equivalent) as indicated by a larger C_{33} than C_{11} in Table 3. Similar results were obtained in a previous theoretical study which also used the model depicted in Fig. 5(b) [18]. The calculated *a*- and *c*-axial moduli ($M_{a,0}$ and $M_{c,0}$ in Table 3) for this structure are very different from our experimental results (comparing values between Tables 2 and 3), indicating that this structure is not suitable for modeling the observed elastic behavior of U_3Si_5. In contrast, the structures shown in Fig. 5(a) and (c) both correctly describe the anisotropic nature of the mechanical properties observed in the

Table 2
2nd order Birch-Murnaghan EOS parameters (bulk modulus, axial linear moduli, ambient unit-cell parameters) for U_3Si_5.

2nd-order Volume BM-EOS		2nd-order Linear BM-EOS *a*-axis		2nd-order Linear BM-EOS *c*-axis	
V_0 (Å^3)	52.60 (11)	a_0 (Å)	3.860 (3)	c_0 (Å)	4.076 (6)
K_0 (GPa)	126 (4)	$M_{a,0}$ (GPa)	173 (8)	$M_{c,0}$ (GPa)	79.7 (4.3)
K_0'	4.0 (fixed)				

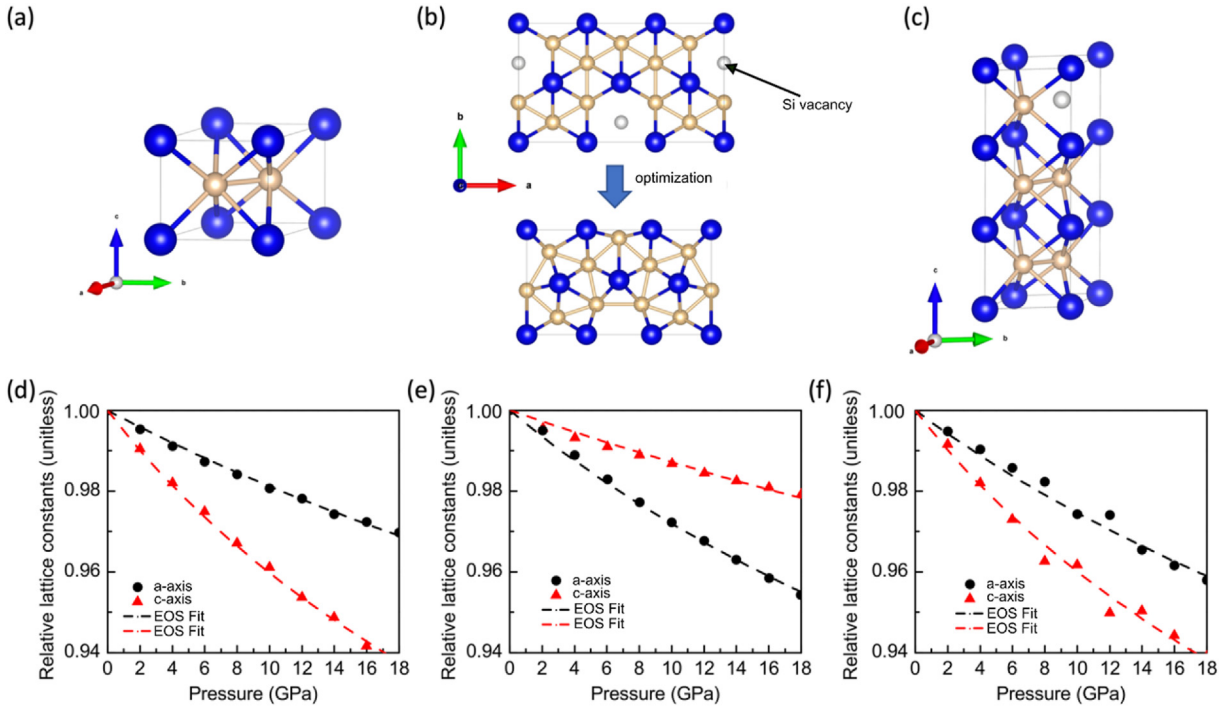

Fig. 5. (a, b, c). Crystal structures used for modeling the mechanical properties of U_3Si_5. (d, e, f) DFT calculated relative lattice constants under pressure for structures in (a, b, c), respectively. Fitted lines indicate equations of state for the *a-axis* (circle) and *c-axis* (triangle) using a linear 2nd order Birch-Murnaghan equation.

Table 3
Calculated mechanical properties of the structures in Fig. 5(a, b, c). $M_{a,0}$ and ($M_{c,0}$) were obtained by fitting the relative lattice constants at high pressures shown in Fig. 5(d, e, f).

In units of GPa	B	C_{11}	C_{22}	C_{33}	C_{44}	C_{55}	C_{66}	C_{12}	C_{13}	C_{23}	$M_{a,0}$	$M_{c,0}$
Structure 1	108.5	180.0	180.0	149.1	90.8	90.8	34.9	110.2	65.9	65.9	157.2	63.5
Structure 2	123.6	196.8	195.8	254.5	154.5	154.5	71.2	51.0	99.3	98.0	98.7	238.6
Structure 3	114.8	183.2	183.2	134.6	83.3	83.3	33.3	116.7	81.9	81.9	111.3	64.1

experiment. However, since the model shown in Fig. 5(a) does not contain Si vacancies and possesses a USi_2 stoichiometry, it does not represent the true structure of U_3Si_5. Therefore, with regard to the mechanical behavior along individual structural directions, the model represented by Fig. 5(c) is the most accurate among the considered structures for U_3Si_5.

This anisotropic behavior may be explained by a closer inspection of the structure of U_3Si_5, shown in Fig. 1. In the *a* direction, there are U–U bonds directly along the *a*-axis, a component of the Si–Si bond (which is parallel to the (001) plane), and a component of the U–Si bond (which is oblique to the *a*- and *c*-axis), all of which contribute to the linear modulus in this direction. In the *c* direction, there are U–U bonds directly along the *c*-axis, yet in contrast to the *a* direction, the only additional contribution in this direction would result from a component of the U–Si bond with no contribution from Si–Si bond. Thus, the contributions to the linear modulus along the *c*-axis would likely be different from those along the *a*-axis. More importantly, if the relative strengths of these bonds are also taken into account, where U–U would be the weakest and Si–Si bonds the strongest, since U–U bonds are metallic and Si–Si bonds are covalent, then the lack of Si–Si bond component in the *c*-axis direction is further consistent with the observed anisotropy, i.e., smaller compressibility along the *a*-axis than along the *c*-axis. Although the details of evolution of the atomic positions with pressure have not been determined, it is qualitatively indicative that the lack of the stronger Si–Si bonds in the *c* direction is responsible for its greater compressibility.

3.3. Bulk modulus

Fig. 6 shows the unit cell volumes of U_3Si_5 as a function of pressure, which are fitted using the Birch-Murnaghan equation of state (BM-EOS) [41]:

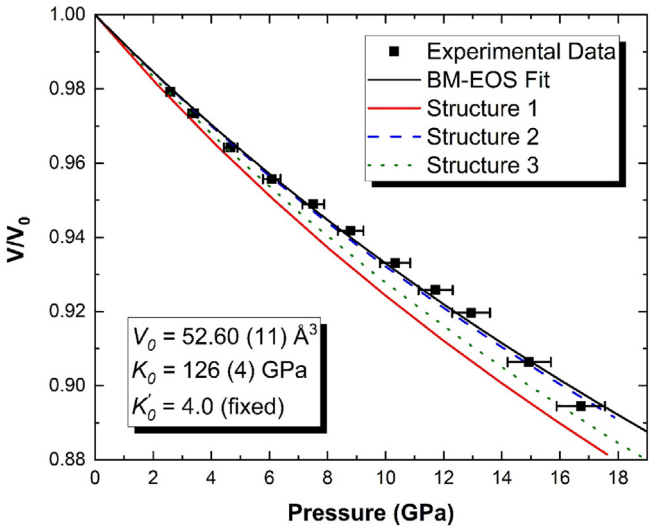

Fig. 6. Relative pressure-volume relation for U_3Si_5 using the unit cell parameters determined by high-pressure XRD. The lines indicate a 2nd-order Birch-Murnaghan equation of state as fitted to the experimental data (solid black line) and those for the three structure models used in DFT calculations. Parameters of the BM-EOS fit to experimental data are given in the bottom inset. The error bars for unit-cell volume values are approximately the size of the data points.

$$P(V) = \frac{3K_0}{2}\left[\left(\frac{V_0}{V}\right)^{\frac{7}{3}} - \left(\frac{V_0}{V}\right)^{\frac{5}{3}}\right]\left\{1 + \frac{3}{4}(K_0' - 4)\left[\left(\frac{V_0}{V}\right)^{\frac{2}{3}} - 1\right]\right\} \quad (2)$$

where V_0 is the zero-pressure cell volume, V is the unit cell volume at high pressure, K_0 is the bulk modulus, and K'_0 is the pressure derivative of the bulk modulus. K'_0 was fixed at a value of 4.0, which simplifies Equation (2) to a 2nd-order BM-EOS. Although a K'_0 value other than 4.0 would be expected for the strong anisotropy observed from the c/a ratio variation, this assumption is made due to the limited pressure range restricting the accuracy of K'_0 determination and has been employed for various materials successfully [42–46]. It is also important to note the effect of the PTM solidification above 11 GPa causing the last two data points to be shifted out of the trend. The optimal values obtained from this fitting are presented in Table 2. Comparing V_0 (52.60 ± 0.11 Å^3) to the literature value for U_3Si_5 (52.17 Å^3) shows a very good agreement, though the fitted value from our experiments are slightly (0.8%) larger [14,15].

Our determined bulk modulus of U_3Si_5 is 126 ± 4 GPa, which is in general agreement with those obtained from DFT calculations by Baskes et al. (102 GPa) and Zhang et al. (111 GPa) [18,19]. Using the same model employed in these previous studies, which is depicted in Fig. 5(b), we obtained a bulk modulus of 123.6 GPa from DFT + U calculations, which is in excellent agreement with our experimentally determined value. However, this structural model does not reproduce the anisotropic behavior that we observed experimentally. In contrast, our DFT + U calculations using the structural models shown in Fig. 5(a) and (c) reproduced the anisotropic behavior and yielded bulk modulus values of 108.5 GPa and 114.5 GPa, respectively, which are both in good agreement with the experimental value. Fig. 6 shows the DFT + U calculated BM-EOS for each structure in addition to the optimal BM-EOS determined from our experimental data. Excellent agreement is noticed between the experimental data and the calculated curve using the structural model in Fig. 5(b), and reasonably good agreement exists between the experimental data and calculated curves using the structural models in Fig. 5(a) and (c). The model in Fig. 5(a) does not properly represent U_3Si_5, resulting in the larger deviations of the calculated curve based on this model from the experimental data compared to the curves obtained based on other structure models (Fig. 6). Comparing the calculated curves based on the other two structure models in Fig. 6, it is clear that the model in Fig. 5(b) provides a better agreement, but due to its inability to reproduce the elastic anisotropy, it is unlikely to be a proper model for U_3Si_5. On the other hand, the model in Fig. 5(c) can reproduce the elastic anisotropy, though it yields a BM-EOS curve that deviates somewhat from the fitted curve to experimental data. A major difference between these two structures lies in the distribution of Si vacancies as depicted in Fig. 5(b) and (c), and thus it is possible that an intermediate structure would be more appropriate to explain the observed mechanical properties of U_3Si_5. Evidence of such an intermediate structure in terms of Si vacancy distribution may be found from high-resolution X-ray/neutron diffraction and various spectroscopic analyses.

It can also be useful to compare the derived bulk modulus with that obtained from the axial linear moduli through the relationship [28]:

$$K_{0,lm} = 3\left(\frac{1}{M_{a,0}} + \frac{1}{M_{a,0}} + \frac{1}{M_{c,0}}\right)^{-1} \quad (3)$$

where $M_{a,0}$ and $M_{c,0}$ are the linear moduli as described in Equation (1). Using the values from Table 2, $K_{0,lm}$ can be calculated using Equation (3), yielding a value of 124.4 ± 13 GPa. This value is in excellent agreement with K_0 determined from the pressure-volume data fitted to the BM-EOS (Table 2).

Although there was no experimental determination in the literature of the bulk modulus of U_3Si_5, a few studies have measured the elastic properties of other U–Si compounds. More specifically, the bulk moduli of USi_2, USi and U_3Si_2 were determined by high-pressure synchrotron XRD using DAC [16,17]. All the experimentally determined K_0 values of U–Si compounds are presented in Table 4. An inspection of these values reveals that U_3Si_5 is the second least compressible of the U–Si compounds studied so far [16,17], and USi_2 is the least compressible with the largest bulk modulus of 140 GPa [16]. Fig. 7 plots the bulk moduli of U–Si compounds (Table 4) as a function of U/(U + Si) ratio. As is shown, with increasing the U/(U + Si) ratio, the bulk modulus of U–Si decreases and thus its compressibility increases. This general trend is consistent with the increased contribution of the weaker U–U metallic bond and decreased contribution of the stronger Si–Si covalent bond, as U/(U + Si) increases.

4. Conclusions

In this study, the high-pressure structural behavior of U_3Si_5 was explored for the first time up to 16.7 GPa using high-energy angle-dispersive synchrotron XRD coupled with diamond anvil cell technique. The unit-cell parameters and cell volume of U_3Si_5 were obtained as a function of pressure. From the pressure dependences of the unit-cell volume and unit-cell parameters a and c, the bulk

Table 4
Comparison of experimentally determined bulk moduli of U–Si compounds.

Compound	K_0 (GPa)
USi_2	140.0 [16]
U_3Si_5	126 (4)*
USi	111.0 [16]
U_3Si_2	107 (6) [17]

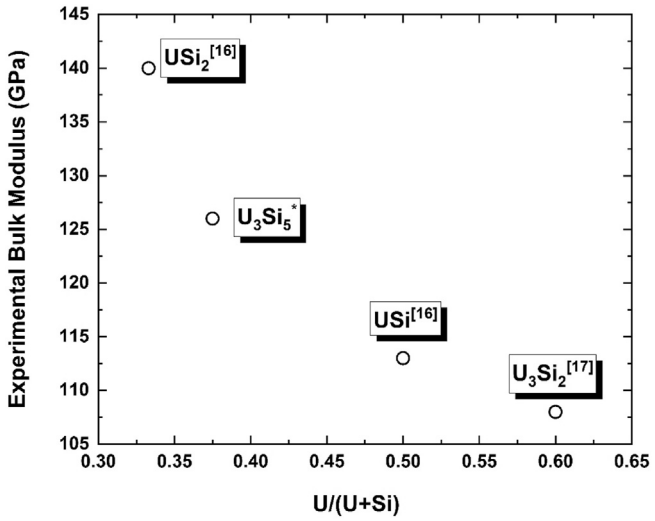

Fig. 7. Comparison of the bulk moduli of various U–Si phases as a function of U/(U + Si). References are given for previously reported data; * indicates this study.

moduli and the axial linear moduli along the a- and c-axis were derived to be: K_0 = 126 ± 4 GPa, $M_{a,0}$ = 173 ± 8 GPa and $M_{c,0}$ = 79.7 ± 4.3 GPa, respectively. Comparison of $M_{a,0}$ with $M_{c,0}$ reveals an anisotropy in compressibility with the *a*-axis being approximately 2.2 times less compressible than the *c*-axis. Moreover, our DFT + U calculations yielded bulk and linear moduli that are comparable to the above experimentally determined values using the hexagonal structure (space group *P6/mmm*). Although previous DFT calculations also gave similar bulk moduli, the structural models used were inappropriate, as they do not reproduce the compressibility anisotropy between the *a*- and *c*-axis. Finally, compilation of all the measured bulk moduli of U–Si phases, including the value of U_3Si_5 determined in this study, reveals that the bulk modulus of U–Si decreases with increasing U/(U + Si) ratio. These obtained elastic parameters and relations provide an important basis for assessing U–Si compounds as accident-tolerant fuels in nuclear reactor applications.

CRediT authorship contribution statement

Jason L. Baker: Methodology, Investigation, Writing - original draft, Visualization. **Gaoxue Wang:** Methodology, Software, Writing - original draft, Visualization. **Tashiema Ulrich:** Methodology, Writing - review & editing. **Josh T. White:** Methodology, Writing - review & editing, Supervision. **Enrique R. Batista:** Methodology, Writing - review & editing, Supervision. **Ping Yang:** Methodology, Writing - review & editing, Supervision. **Robert C. Roback:** Supervision. **Changyong Park:** Methodology, Writing - review & editing. **Hongwu Xu:** Conceptualization, Methodology, Writing - review & editing, Supervision, Project administration, Funding acquisition.

Declaration of competing interest

The authors declare that they have no known competing financial interests or personal relationships that could have appeared to influence the work reported in this paper.

Acknowledgements

Research presented in this article was supported by the Laboratory Directed Research and Development (LDRD) program at Los Alamos National Laboratory (LANL) under project number 20180007. JLB acknowledges the support of the Seaborg Institute through a LANL Seaborg postdoctoral fellowship. The authors would like to thank Andrew J. Gaunt for useful discussions and comments. LANL, an affirmative action/equal opportunity employer, is managed by Triad National Security Administration of the U.S. Department of Energy under contract number 89233218CNA000001. High-P synchrotron XRD experiments were performed at HPCAT (Sector 16), Advanced Photon Source (APS), Argonne National Laboratory. HPCAT operations are supported by DOE-NNSA's Office of Experimental Sciences. The Advanced Photon Source is a U.S. Department of Energy (DOE) Office of Science User Facility operated for the DOE Office of Science by Argonne National Laboratory under Contract No. DE-AC02-06CH11357.

Data availability

The raw/processed data required to reproduce these findings cannot be shared at this time due to technical or time limitations.

Appendix A. Supplementary data

Supplementary data to this article can be found online at https://doi.org/10.1016/j.jnucmat.2020.152373.

References

[1] A. Nelson, J. White, D. Byler, J. Dunwoody, J. Valdez, K. McClellan, Overview of properties and performance of uranium-silicide compounds for light water reactor applications, Trans. Am. Nucl. Soc. 110 (2014) 987–989.
[2] J.T. White, A.T. Nelson, D.D. Byler, D.J. Safarik, J.T. Dunwoody, K.J. McClellan, Thermophysical properties of U_3Si_5 to 1773 K, J. Nucl. Mater. 456 (2015) 442–448.
[3] J.T. White, A.T. Nelson, J.T. Dunwoody, D.D. Byler, D.J. Safarik, K.J. McClellan, Thermophysical properties of U_3Si_2 to 1773 K, J. Nucl. Mater. 464 (2015) 275–280.
[4] J.T. White, A.T. Nelson, J.T. Dunwoody, D.D. Byler, K.J. McClellan, Thermophysical properties of USi to 1673 K, J. Nucl. Mater. 471 (2016) 129–135.
[5] T. Wang, N. Qiu, X. Wen, Y. Tian, J. He, K. Luo, X. Zha, Y. Zhou, Q. Huang, J. Lang, First-principles investigations on the electronic structures of U_3Si_2, J. Nucl. Mater. 469 (2016) 194–199.
[6] E.S. Wood, J.T. White, A.T. Nelson, Oxidation behavior of U-Si compounds in air from 25 to 1000 °C, J. Nucl. Mater. 484 (2017) 245–257.
[7] X. Guo, J.T. White, A.T. Nelson, A. Migdisov, R. Roback, H. Xu, Enthalpy of formation of U_3Si_2: a high-temperature drop calorimetry study, J. Nucl. Mater. 507 (2018) 44–49.
[8] H. Vaugoyeau, L. Lombard, J. Morlevat, Contribution a l'etude du diagramme d'equilibre uranium silicium, J. Nucl. Mater. 39 (1971) 323–329.
[9] Y. Sasa, M. Uda, Structure of stoichiometric USi_2, J. Solid State Chem. 18 (1976) 63–68.
[10] N.R. Brown, A. Aronson, M. Todosow, R. Brito, K.J. McClellan, Neutronic performance of uranium nitride composite fuels in a PWR, Nucl. Eng. Des. 275 (2014) 393–407.
[11] H. Okamoto, in: second ed., in: T. Massalski (Ed.), Binary Alloy Phase Diagrams, vol. 3, ASM International, 1990, pp. 3374–3375.
[12] X. Lü, Y. Wang, C.C. Stoumpos, Q. Hu, X. Guo, H. Chen, L. Yang, J.S. Smith, W. Yang Y. Zhao, Enhanced structural stability and photo responsiveness of $CH_3NH_3SnI_3$ perovskite via pressure-induced amorphization and recrystallization, Adv. Mater. 28 (2016) 8663–8668.
[13] G. Bounos, M. Karnachoriti, A.G. Kontos, C.C. Stoumpos, L. Tsetseris, A. Kaltzoglou, X. Guo, X. Lü, Y.S. Raptis, M.G. Kanatzidis, Defect perovskites under pressure: structural evolution of Cs_2SnX_6 (X= Cl, Br, I), J. Phys. Chem. C 122 (2018) 24004–24013.
[14] N. Sato, M. Kagawa, K. Tanaka, N. Takeda, T. Satoh, T. Komatsubara, Magnetic properties of a mass-enhanced ferromagnet U_2PtSi_3, J. Magn. Magn Mater. 108 (1–3) (1992) 115–116.
[15] K. Remschnig, T.L. Bihan, H. Nöel, P. Rogl, Structural chemistry and magnetic behavior of binary uranium silicides, J. Solid State Chem. 97 (2) (1992) 391–399.
[16] S. Yagoubi, S. Heathman, A. Svane, G. Vaitheeswaran, P. Heines, J.-C. Griveau, T.L. Bihan, M. Idiri, F. Wastin, R. Caciuffo, High pressure studies on uranium and thorium silicide compounds: experiment and theory, J. Alloys Compd. 546 (2013) 63–71.
[17] X. Guo, X. Lü, J.T. White, C.J. Benmore, A.T. Nelson, R.C. Roback, H. Xu, Bulk moduli and high pressure crystal structure of U_3Si_2, J. Nucl. Mater. 523 (2019) 135–142.

[18] X. Zhang, J. Lang, Q. Huang, T.C. Germann, Y. Qiao, J. Ding, H. Gao, S. Du, Electronic structures, mechanical properties and defect formation energies of U_3Si_5 from density functional theory calculations, Prog. Nucl. Energy 116 (2019) 87–94.
[19] M.I. Baskes, D. Andersson, Assessment of Semi-empirical Potentials for the U-Si System, FY2016. No. LA-UR-15-26949. Los Alamos National Laboratory, Los Alamos, NM USA.
[20] C.K. Chung, X. Guo, G. Wang, T.L. Wilson, J.T. White, A.T. Nelson, A. Sheylug, H. Boukhalfa, P. Yang, E.R. Batista, A.A. Migdisov, R.C. Roback, A. Navrotsky, H. Xu, Enthalpies of formation and phase stability relations of USi, U_3Si_5 and U_3Si_2, J. Nucl. Mater. 523 (2019) 101–110.
[21] R. Hrubiak, S. Sinogeikin, E. Rod, G. Shen, The laser micro-machining system for diamond anvil cell experiments and general precision machining applications at the High Pressure Collaborative Access Team, Rev. Sci. Instrum. 86 (2015), 072202.
[22] H.K. Mao, J. Xu, P.M. Bell, Calibration of the ruby pressure gauge to 800 kbar under quasi-hydrostatic conditions, J. Geophys. Res. 91 (1986) 4673–4676.
[23] S. Klotz, J.C. Chervin, P. Munsch, G.L. Marchand, Hydrostatic limits of 11 pressure transmitting media, J. Phys. D Appl. Phys. 42 (2009), 075413.
[24] C. Prescher, V.B. Prakapenka, Dioptas: a program for reduction of two-dimensional x-ray diffraction data and data exploration, High Pres. Res. 35 (2015) 223.
[25] A. Le Bail, Whole powder pattern decomposition methods and applications: a retrospection, Powder Diffr. 20 (4) (2005) 316–326.
[26] A. Le Bail, Extracting structure factors from powder diffraction data by iterating full pattner profile fitting, in: Accuracy in Powder Diffraction II, NIST Special Publication, 1992, p. 846.
[27] B. Hunter, Rietica - A visual Rietveld program No. 20, International Union of Crystallography Commission on Powder Diffraction Newsletter, 1998. http://www.rietica.org.
[28] J. Gonzalez-Platas, M. Alvaro, F. Nestola, R. Angel, EosFit7-GUI: a new graphical user interface for equation of state calculations, analyses, and teaching, J. Appl. Crystallogr. 49 (2016) 1377–1382.
[29] R.J. Angel, M. Alvaro, J. Gonzalez-Platas, EosFit7c and a Fortran module (library) for equation of state calculations, Z. für Kristallogr. - Cryst. Mater. 229 (2014) 405–419.
[30] G. Kresse, D. Joubert, From ultrasoft pseudopotentials to the projector augemented-wave method, Phys. Rev. B 59 (1999) 1758–1775.
[31] G. Kresse, J. Furthmüller, Efficiency of ab-initio total energy calculations for metals and semiconductors using a plane-wave basis set, Comput. Mater. Sci. 6 (1996) 15–50.
[32] J.P. Perdew, K. Burke, M. Ernzerhof, Generalized gradient approximation made simple, Phys. Rev. Lett. 77 (1996) 3865–3868.
[33] S. Dudarev, G. Botton, S. Savrasov, C. Humphreys, A. Sutton, Electron-energy-loss spectra and the structural stability of nickel oxide: an LSDA+ U study, Phys. Rev. B 57 (1998) 1505–1509.
[34] M.J. Noordhoek, T.M. Besmann, D. Andersson, S.C. Middleburgh, A. Chernatynskiy, Phase equilibria in the U-Si system from first-principles calculations, J. Nucl. Mater. 479 (2016) 216–223.
[35] T. Miyadai, H. Mori, Y. Tazuke, T. Komatsubara, Magnetic and electrical properties of the U-Si system, J. Magn. Magn Mater. 90–91 (1990) 515–516.
[36] H. Weitzel, C. Keller, Neutronenbeugungsuntersuchungen an $(SE_{0.5}U_{0.5})O_2$ (SE = Y, La, Nd, Ho, und Lu), J. Solid State Chem. 13 (1–2) (1975) 136–141.
[37] Y. Zhang, P. Liu, Y. Xian, X. Wang, L. Sheng, P. Zhang, Electronic structure of AlB_2-type U-Si binary intermetallic compounds by hybrid density functional calculations, J. Phys. Sci. Appl. 6 (6) (2016) 12–19.
[38] H. Xu, Y. Zhao, J. Zhang, D.D. Hickmott, L.L. Daemen, In situ neutron diffraction study of deuterated portlandite $Ca(OD)_2$ at high pressure and temperature, Phys. Chem. Miner. 34 (2007) 223–232.
[39] A. Brown, J.J. Norreys, Uranium disilicide, Nature 191 (1961) 61–62.
[40] M. Ångqvist, W.A. Muñoz, J.M. Rahm, E. Fransson, C. Durniak, P. Rozyczko, T.H. Rod, P. Erhart, ICET – A Python library for constructing and sampling alloy cluster expansions, Adv. Theory Simul. 2 (2019) 1900015.
[41] F. Birch, Finite elastic strain of cubic crystals, Phys. Rev. 71 (1947) 809–824.
[42] S. Wang, X. Yu, J. Zhang, Y. Zhang, L. Wang, K. Leinenweber, H. Xu, D. Popov, C. Park, W. Yang, D. He, Y. Zhao, Crystal structures, elastic properties, and hardness of high-pressure synthesized CrB_2 and CrB_4, J. Superhard Mater. 36 (4) (2014) 279–287.
[43] Y. Wang, J. Zhang, H. Xu, Z. Lin, L.L. Daemen, Y. Zhao, L. Wang, Thermal equation of state of copper studied by high P-T synchrotron x-ray diffraction, Appl. Phys. Lett. 94 (2009), 079104.
[44] J. Zhu, H. Xu, J. Zhang, C. Jin, L. Wang, Y. Zhou, Thermal equations of state and phase relation of $PbTiO_3$: a high P-T synchrotron x-ray diffraction study, J. Appl. Phys. 110 (2011), 084103.
[45] H. Xu, J. Zhang, Y. Zhao, G.D. Guthrie, D.D. Hickmott, A. Navrotsky, Compressibility and pressure-induced amorphization of guest-free melanophlogite: an in-situ synchrotron x-ray diffraction study, Am. Mineral. 92 (2007) 166–173.
[46] J. Zhu, J. Zhang, H. Xu, S.C. Vogel, C. Jin, J. Frantti, Y. Zhao, Pressure-induced reversal between thermal contraction and expansion in ferroelectric $PbTiO_3$, Sci. Rep. 4 (1) (2014) 1–6.